Article

Grain-Level Numerical Simulations for the Effective Elasticity of Weakly Cemented Sandstones
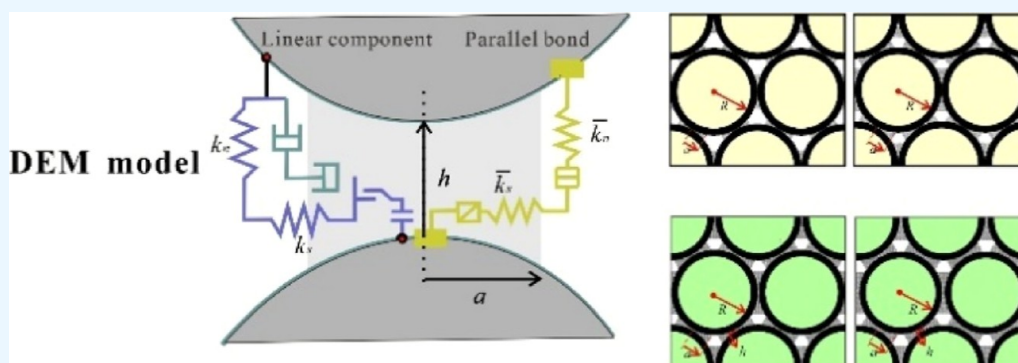
Xiaoyi Xu*

Read Online

ACCESS | ᴵᴵᴵ Metrics & More | 🅴 Article Recommendations

ABSTRACT: Weakly cemented sandstones are characteristic of loose-bonding contacts, large porosities, and high-clay contents. This study presents a discrete element method (DEM)-based numerical study for the effective elasticity of such rocks that mainly depends on the mechanical behavior of intergranular contact regions. The DEM scheme employs a set of normal and shear springs to phenomenologically describe the mechanical behavior of intergranular finite-sized cements defined by three morphological parameters: cement thickness, bonding radius, and grain radius. Applications to two digital models established in terms of contact-bonding and distant-bonding modes, respectively, where spherical quartz grains are randomly packed together with adding cements under the specified confining pressure, are compared with the theoretical predictions by the contact-bonding and distant-bonding cement theories, which demonstrates a good agreement generally for small contact widths, small contact thicknesses, and large-magnitude moduli, especially for the effective shear modulus. Applications to a series of artificial sandstone samples made in terms of different proportions of quartz grains and clays (a mixture of epoxy and kaolinite) under loose compaction for weak cementation demonstrate a good agreement with ultrasonic measurements. Numerical investigations for the micromechanical characteristics (differential stress fields, force chains, and fabric tensors) of artificial samples subject to applied axial strains demonstrate that the strong mechanical behavior of weakly cemented sandstones tends to appear inside the cohesive aggregates of stiff grains because of their relatively large sizes with loose compaction.

1. INTRODUCTION

Grain contact domains are most sensitive to deformations. As the pore space of porous rocks, such intergranular structures are molded by compaction, dissolution, and cementation during diagenesis and compose of the origin of rock elasticity. The strength of rocks depends strongly on intergranular cements. Therefore, the elastic characteristics of rocks are mainly affected by the mechanical property and geometry of intergranular structures, especially for weakly cemented (unconsolidated) sands which are very common in sedimentary deposits. As the main elements of heavy oil reservoirs, such loose sands are characteristic of large porosities, loose cementations, and high clay contents.

The key issue in cemented sands is highly relevant to the mechanical behavior at grain contacts between bonds. There have been numerous analytical models to describe the elasticity

of consolidated rocks, which potentially tend to overestimate acoustic velocities for poorly cemented sands. There have existed some models that are developed based on the microstructural contact of unconsolidated sands and estimate effective moduli from the contact stiffness between grains. Classical Hertz−Mindlin (HM) model describes the mechanical behavior of grain-to-grain elastic interactions for randomly packed spherical grains,[1] which assumes a small contact area
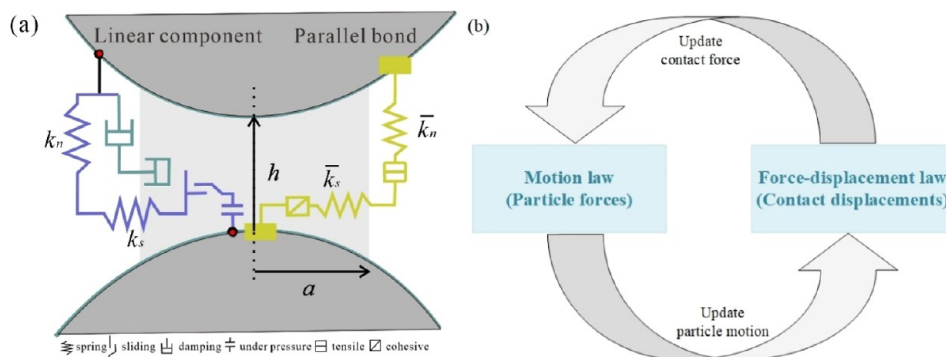
Figure 1. (a) Parallel bond model (cross section) using normal and shear springs at a cemented contact region (marked by light gray area) between distant grains, where a and h denote the radius and thickness of the cement cylinder, respectively. (b) Calculation cycle flowchart of any DE that connects with normal and shear springs at contact surfaces.

compared with the dimension of grains. The HM model initiates numerous theoretical works for granular media. For instance, Dvorkin and Nur (1996)[2] extended the HM model to low-porosity unconsolidated sandstones by incorporating the Hashin–Shtrikman (HS) lower bound for effective moduli up to critical porosity. Madadi and Christy (2012)[3] modify the CPA model to include grain-contact moduli and coordination-number effect. However, many of these works focus on uncemented grains that are directly bonded together by a normal loading stress to keep contact.

Using the apparent microstructure of poorly cemented sands, Dvorkin et al. (1991 and 1994)[4,5] proposed a contact cement theory (CCT) to represent the effect of cements on the normal and tangential stiffness of spherical grains, which is revisited by Langlois and Jia (2014)[6] and Langlois (2015)[7] for an accurate approximate expression of contact stiffnesses. Grains in the CCT model are directly bonded together by a few intergranular cements near the contact area. It is worth noting that the small quantity of cementation by even very soft cements can significantly increase the stiffness of sands.[2,8] Chiu et al. (2017)[9] used the CCT model to develop a biconcave bond model to study the effect on the mechanical behavior of rocks. The CCT model usually holds for high porosity because of the minor amount of cement at grain contacts. As indicated by Theocharis et al. (2020),[10] the model does not consider the dependence of coordination numbers on the cement content. By combining the CCT, HM, and HS models as well as including the intergranular volume index (IGV) for pressure effects,[11] a patchy cement model[12,13] has been developed to predict stress dependence in poorly consolidated sandstones with weak cementation. A comprehensive comparison of various analytical models can be referred to the work of Carcione et al. (2022).[14] It should be stressed that the CCT model is based on the grain-to-grain direct contact with a small cemented contact region. Unconsolidated sandstones with weak cementation are usually characteristic of nonzero contact thickness between adjacent grains, which will reduce the normal and tangential stiffnesses.[8] Therefore, the CCT model tends to overestimate the elastic moduli of weakly cemented sands.[12] Xue-Hui et al. (2014)[8] modify the CCT model with basal cementation (i.e., bridging cementation) to consider the effect of contact thickness. The modified CCT model (MCCT) has been used to examine the acoustic velocities for heavy oil sands.[15] In this study, the CCT and MCCT analytical models will be validated by a numerical scheme.

Many distant contact problems have no analytical solution, resulting in the development of various numerical methods which are generally classified into two categories: continuum- and discrete-based models. The former has been widely used for effective elasticity prediction because of their computational efficiency by regarding the rocks as continuous granular media. It is worth mentioning that Madadi and Saadatfar (2017)[16] present a finite-element simulation for the effective elastic moduli of unconsolidated sandstones by varying the volume fraction of grain contacts. However, such cemented media as rocks are natural to handle using discrete-based methods, for example, discrete element methods (DEMs) that can specifically account for individual factors (e.g., granular texture, particle kinematics, and force transmission) that influence the mechanical behavior of rocks. Particularly, for fractured rocks, the DEM seems more suitable[17−20] where even a small number of cracks have significantly effect on the elastic properties of rocks. A discrete fracture network (DFN) to model complex fractures has been coupled with the DEM for strength characterization of fractured rocks.[21] Xu et al. (2021)[22] present a DEM−DFN crack inversion for the distribution of coordination numbers, which captures the structural characteristics of fractures. On the other hand, the DEM is an efficient numerical method to investigate the micromechanism of deformations in cemented rocks,[23−25] elastic characteristics,[26−28] and size-dependent wave propagation.[29] The key is relevant to bonded particle models.[30−34] The methods can be extended to poorly cemented rocks by weakening the strength of bonds at grain contacts.[35,36] The aforementioned numerical studies focus on the mechanical behavior of bonded particle models by adopting various forms of contact laws. Theocharis et al. (2020)[10] attempt the accurate elasticity of bonding cementation by extending the analytical contact-bonding model of Langlois (2015)[7] to distant-bonding cases. They conduct a DEM-based numerical study to elaborate the effect of bonding parameters on the elastic characteristics of these two typical cemented bonds (contact bonding and distant bonding). For the distant-bonding model, noncontacting grains are joined by a cement bridge (i.e., basal cementation or bridging cementation).

The research aims to develop a DEM-based numerical scheme for the effective elasticity of weakly cemented sands based on the PFC2D platform (Itasca, 2014) in which a built-in parallel bond model (PBM) can be applied to the bridging cementation. It describes the mechanical behavior of a finite-sized cement material deposited between two grains. The process is two steps.
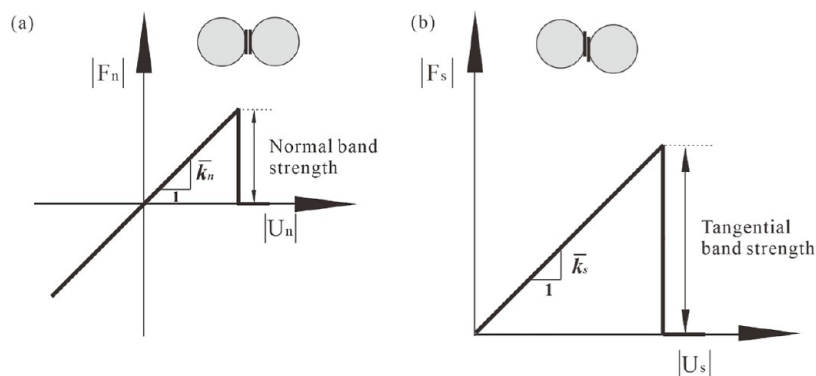
Figure 2. Parallel-bond force–displacement law for normal force vs normal displacement (a) and shear force vs tangential displacement (b).
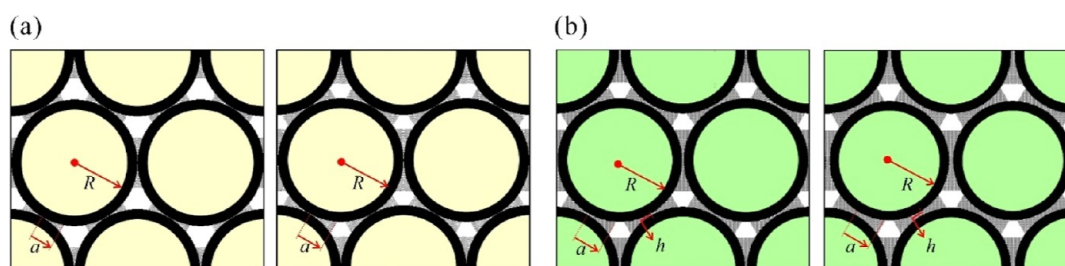

Figure 3. DE arrangements in terms of the contact-bonding (a) and distant-bonding (b) patterns, with the intergranular cementation size and matrix porosity controlled by the key parameters a, R, and h.

First, this essay develops the DEM-based numerical scheme to approximate the contact-bonding and distant-bonding functions based on the built-in PBM and assumes that both grains and cements are linear, elastic, and isotropic. The scheme is validated by the theoretical CCT and MCCT solutions for isotropically confined bead packs assembled in terms of the contact-bonding and distant-bonding modes, respectively. Second, a series of weakly cemented clay-bearing sandstone samples are artificially made with different packing textures by increasing the proportion of clay contents under a small fixed confining pressure. Based on scanning electron microscopic (SEM) images from these sandstone samples, the grain mineral formations and grain contacts can be measured.[3] The mineral formation of cements and their volume fraction of each mineral can be identified.[37] Based on the digital SEM images of these differently packed samples, this article numerically calculates their effective bulk and shear moduli, which are validated by quantitative confrontations with ultrasonic experiments to the artificial sandstone samples. In addition, this research also further examine the effect of differential stresses, force chains, and fabric tensors on the elastic properties of cemented sandstones subject to biaxial compression tests.

2. NUMERICAL METHODS AND PROCEDURE

2.1. DEM Model. The DEM has made significant advances in complex simulations of granular media and aggregates but focusing on the mechanical behavior of intergranular cementation in soft and hard rocks. The PBM built in the PFC2D provides an efficient approach to improve significantly the predictive capability of the DEM for rock-modeling purpose. It realistically captures the macroscopic response to dynamic or kinematic boundary conditions in terms of microscale bonded structures. In this study, the built-in PBM in the PFC2D to establish a grain-level numerical scheme for modeling the effective elasticity of weakly cemented sandstones is employed,
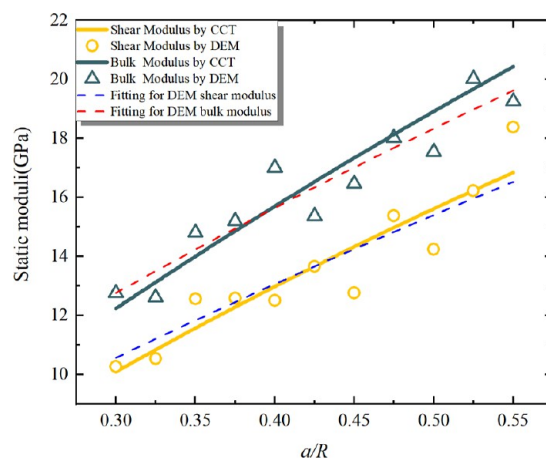

Figure 4. Comparison of the analytical and simulated bulk and shear moduli vs the dimensionless parameter a/R for contact-bonding DEs.

which will be compared with the theoretical CCT and MCCT solutions and validated by ultrasonic experiments.

2.2. Parallel Bond Model. The PBM describes the mechanical behavior of granular finite-sized cements to model the contact-bonding and distant-bonding functions. It can be equivalized by elastic springs with normal and shear stiffnesses, as shown in Figure 1a, where the parallel-bond component works with the springs of the linear component to build up an elastic interaction between two grains. The linear model does not resist relative rotation. It accommodates a slip by imposing a Coulomb limit on the shear force. The PBM resists relative rotation but is linear elastic until the strength limit before the bond breaks. Relative motions at intergranular contact regions induce force and moment within the bond material. If the resulting maximum normal or shear stresses exceed its corresponding bond strength, the parallel bond breaks and
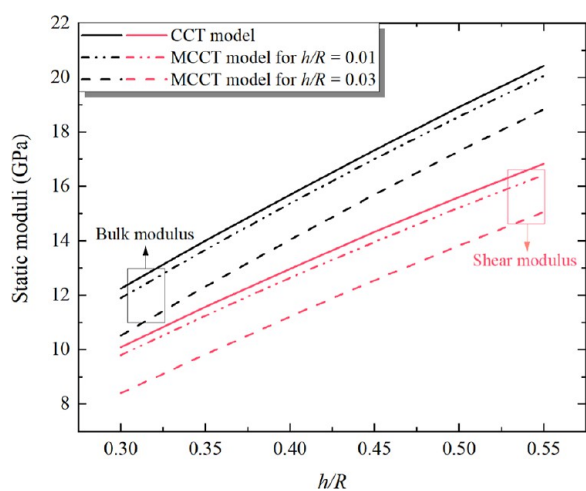
Figure 5. Comparison of the bulk and shear moduli vs the dimensionless parameter a/R for the packing models with different cemented thicknesses.
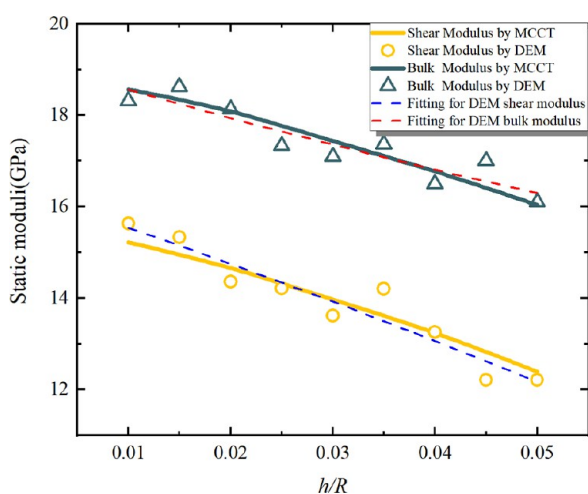

Figure 6. Comparison of the elastic moduli vs the dimensionless parameter h/R for the packing models with different cemented thicknesses.

becomes unbonded. The unbonded PBM is equivalent to the linear model. The DEM calculation process involves two steps, as shown in Figure 1b. The first step is to calculate the interaction forces between DEs according to the force–displacement law. Second, the velocity and position of each DE are updated based on Newton's law of motion.

The force–displacement law applied to each DE to update the contacting force resorts to a local constitutive law, with its mechanical behavior of normal and shear springs generally expressed in Figure 2. The essence of the problem is to estimate the distribution of normal and tangential tractions, which satisfies the normal and tangential boundary conditions at the interface. The total contact force consists of the linear force, the dashpot force, and the parallel bond force. The linear and dashpot forces are updated using the linear model through the blue springs in Figure 1a, and the force and moment are updated using the PBM through the yellow springs in the figure. The parallel-bond force is decomposed into a normal and shear force, with its moment into a twisting and bending moment. The parallel bond has the advantage over a simple contact bond in that it acts together with the normal contact spring and transmits

moment by compressive and tensile loads. Therefore, it can realistically model the effect of natural cements. Unlike the CCT model,[4,5,7] the contact constitutive law in the parallel bond is of a wide applicability for more complex simulations of granular media. It allows to model a very large number of particles.

Weakly cemented sands are conceived as an assemblage of particles packed in terms of the contact-bonding and distant-bonding modes, with additional cements deposited around intergranular contact regions. The PBM phenomenologically describes the contact behavior of cemented particles for numerical computations. The matrix of intact rocks is regarded as an elastic, homogeneous, and isotropic medium. Figure 3 shows the arrangement of packed particles in terms of the contact-bonding and distant-bonding modes. This study can control the intergranular cementation size and matrix porosity by assigning the parameters a, R, and h with different values. These packed particles will be used to discretize digital image pixels of sandstone samples, with the coordinates of particles set by the approximate zone of the pixels within the digital core image. The relevant micromechanical parameters of DEs can be adjusted to the mechanical properties of the approximate zone.

2.3. Validation by the CCT Model for Contact-Bonding Cementation. This work applies the aforementioned DEM numerical scheme to a quartz-grain packing model with weak contacts by the contact-bonding mode. The static elastic moduli (bulk and shear) of grains and cements are assumed to be (38, 44) and (15, 8) GPa, respectively. The critical porosity of loosely packed grains is assumed to be approximately 0.36 which is similar to that of randomly packed spherical grains.[2] The effective bulk and shear moduli are numerically calculated for the dimensionless parameter a/R ranging from 0.3 to 0.55.

This work first packs spherical grains randomly and uses the servo function to balance the sample under the specified confining pressure that mechanically stabilizes these packed DEs to ensure the contact-bonding mode. The resulting DE model of spherical grains has an isotropic distribution of grain contacts, as shown in Figure 3a. Then, this work adds cements to individual intergranular contact regions for the expected value of a/R and carries out repeated uniaxial compression tests for a stable simulation of Young's modulus and Poisson's ratio of isotropic material. Based on the analytical formula of CCT,[2] the effective bulk and shear moduli of the same model can also be calculated. The algorithm of CCT is presented in Appendix A. Figure 4 compares the analytical and simulated moduli for the dimensionless parameter a/R ranging from 0.3 to 0.55. Due to the large uncertainty and randomness in the parameter calibration of numerical simulation, the numerical results are usually not completely consistent with the theoretical results. The simulation results in this paper are slightly different from the theoretical prediction results, but in general, they still show a high consistency. Both shear moduli and bulk moduli increase with the increase of bonding width, which reflects the increase of bond strength of the whole system. This trend can be intuitively understood: the porosity decreases with the increase of a/R ratio, and the greater the a/R ratio, the greater the contact stiffness of the system, which is manifested as an increase in bond strength and an increase in equivalent elastic moduli.

Similar to the validation for contact-bonding DEs by the CCT model, the DEM numerical scheme is applied to a quartz-grain packing model with weak contacts by the distant-bonding mode. The static elastic moduli (bulk and shear) of grains and cements are assumed to be (38, 44) and (6.8, 2.0) GPa, respectively. This research chooses cement materials with smaller moduli. The
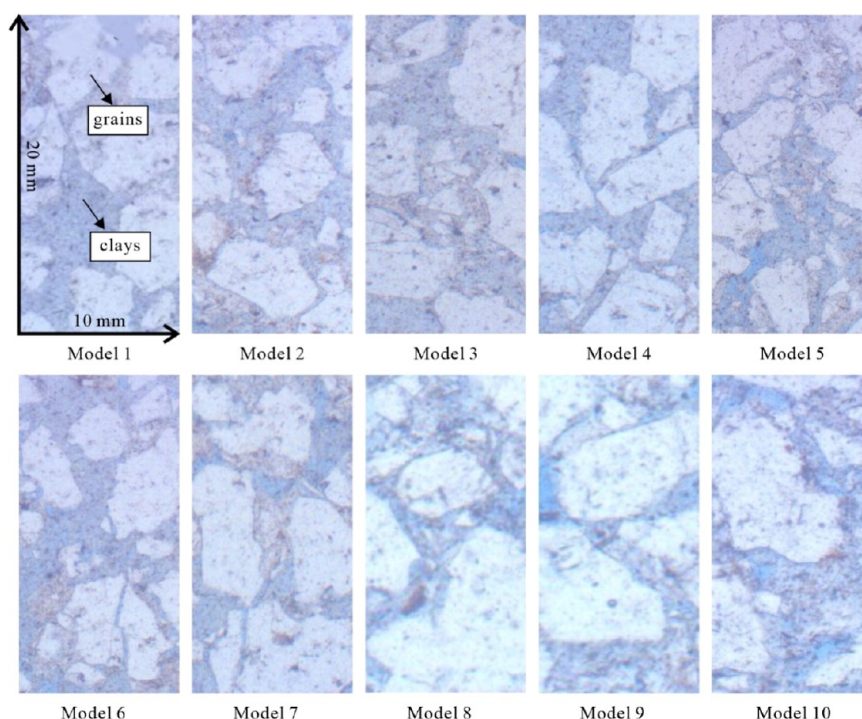
Figure 7. SEM images of 10 sandstone samples synthesized in terms of different proportions of grains and clays under limited confining pressures for weak cementation, showing granular aggregates as the skeleton and filled clays as cements.

effective elastic moduli are numerically calculated for the dimensionless parameter h/R ranging from 0.01 to 0.05. The distant-bonding DEs packed with different cemented thicknesses under the specified confining pressure present an isotropic distribution of grains and bridging cement materials, as shown in Figure 3b.

Accounting to the analytical formula of MCCT[8] detailed in Appendix A, this study compute the effective elastic moduli of the packing models with different cemented thicknesses and the analytical solutions of samples of the CCT model and MCCT model, as shown in Figure 5. As can be seen from the figure, under the influence of cementation thickness, the modulus of based-type cementation is slightly lower than that of porous cementation under the same cementation radius. The reason is that the increase of the central thickness of the cement will reduce the normal contact stiffness and tangential contact stiffness, resulting in relatively soft sandstone, so the modulus decreases. Based on this, the fixed cement width a/R value in the simulation process is 0.50. The modulus value of basement-cemented sandstone under variable cementation thickness (h/R, h is the cementation thickness and R is the cementation radius) is simulated through the uniaxial compression test in the Y direction, and only the linear elastic change stage is still concerned. As shown in Figure 6, the simulation results in this paper are slightly different from the analytical prediction results, but in general, they still show a high consistency. When the fixed cement width a/R is 0.50, the weakly cemented sandstone becomes relatively soft with the increase of contact thickness, so the overall stiffness and effective modulus of the system decrease with the increase of contact thickness.

3. NUMERICAL EXPERIMENTS

Natural cemented sandstones are generally complex in mineral formations and microstructures that involve with complicated interactions between the base and cements. In contrast,
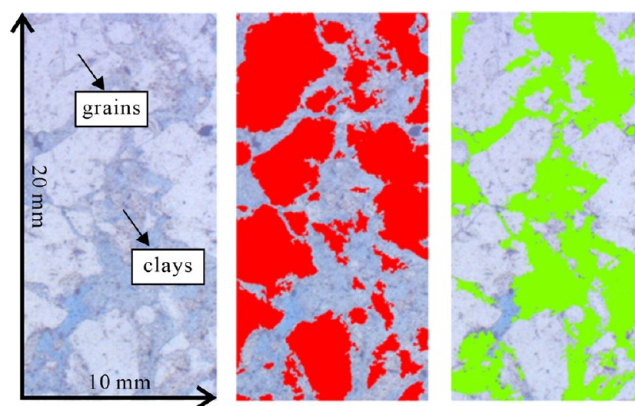

Figure 8. Cohesive aggregates of grains (marked in red) and clays (marked in green) for model 5 (left panel), identified by image processing in terms of the pixel grayscale of grains and clays in the SEM image.

Table 1. Basic Petrophysical Properties and Ultrasonic Measurements for Artificially Made Sandstones

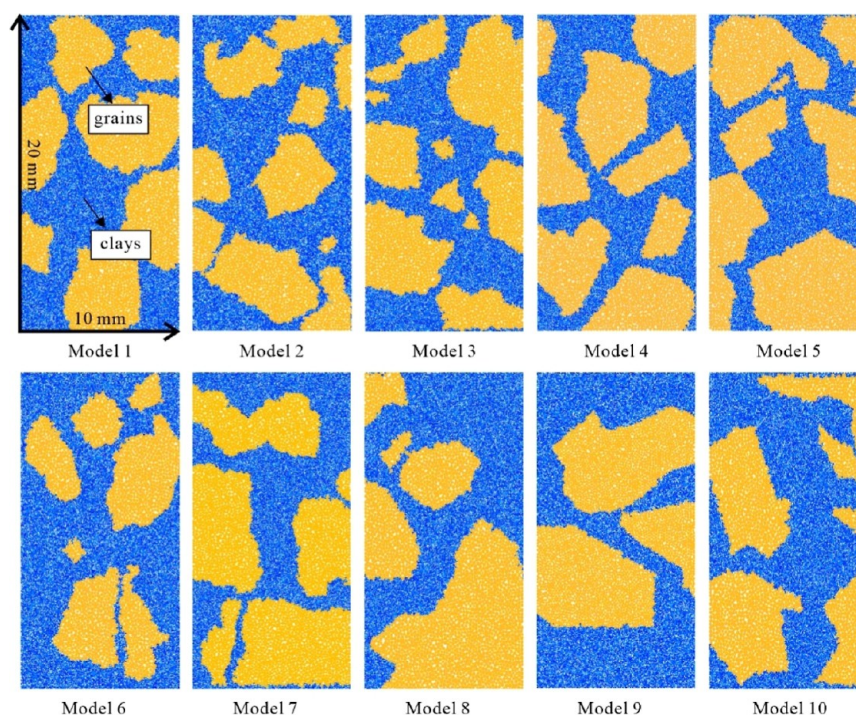| sample	clay content	porosity	density (g·cm⁻³)	V_p (m·s⁻¹)	V_s (m·s⁻¹)
1	0.09	0.31	1.64	1897	1219
2	0.11	0.29	1.69	1856	1347
3	0.25	0.15	2.07	2521	1384
4	0.24	0.16	2.05	2505	1449
5	0.26	0.15	2.09	2320	1525
6	0.18	0.22	1.89	2190	1385
7	0.22	0.18	1.96	2392	1519
8	0.23	0.17	2.03	2436	1425
9	0.25	0.15	2.08	2442	1491
10	0.15	0.25	1.76	2130	1482

Figure 9. Digital models of DEs for 10 sandstone samples shown in Figure 7, where cohesive aggregates of grains (marked in yellow) and clays (marked in blue) are approximated by different-sized DEs with specific geometrical and micromechanical parameters for the mechanical behavior of individual voxels.
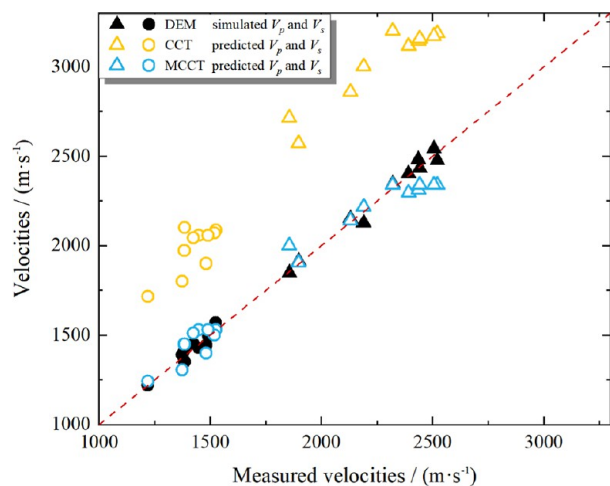

Figure 10. Cross plot of measured velocities against DEM-simulated and CCT-predicted velocities, respectively.

synthetic clay-bearing sandstones present known grains, cements, and their proportions, which are packed under the controllable confining pressure. In this study, artificial sandstone samples are preferred to test numerical approaches for effective elasticity, which is validated by ultrasonic experiments.

3.1. Artificial Sandstone Samples and Ultrasonic Measurements. Artificial sandstones consist of quartz grains and cements (a mixture of epoxy and kaolinite). These components with irregular shapes are packed under limited confining pressures for weak cementation. The static elastic moduli (bulk and shear) of grains and cements are 38, 44 and 2.24, 1.57 GPa, respectively, with their densities measured by a helium porosimeter as 2.65 and 1.38 $g \cdot cm^{-3}$, respectively. The resulting critical porosity of loosely cemented grains is measured

to be approximately 0.4. This research makes 10 sandstone samples in terms of different proportions of grains and cements, with each as 10 and 20 mm in width and height, respectively. Figure 7 shows the SEM images of the resulting sandstone samples and represents that these thin-sheet images basically capture the microstructural features of natural cemented sandstones. Cohesive aggregates of grains with different shapes and scales in size are randomly embedded in the clays. Intergranular contact regions are filled with cements varying in thickness and shape, which manifests both the contact-bonding and distant-bonding modes for weak contacts.

Based on the pixel grayscale of grains and cements in the SEM images, the threshold segmentation of these two components can be easily implemented by image processing, enabling the accurate extraction of grains and clays. Figure 8 shows cohesive aggregates of grains (marked in red) and clays (marked in green) for model 5. Based on the pixel recognition of grains and clays, the petrophysical properties such as clay content and porosity for each sample can be estimated, as listed in Table 1. Ultrasonic measurements are conducted to each sample using 1 and 0.5 MHz for P- and S-wave piezoelectric transducers (PZTs), respectively. The resulting P- and S-wave velocities are listed in Table 1. Furthermore, this study can identify grain-contact area distributions, based on which the statistical analysis of grain contacts results in the normalized cement thickness ranging from 0.0 to 0.05, with normalized cementation radii and coordination numbers estimated by the method.[37]

3.2. DEM Numerical Simulations Based on Digital Image Pixels. For elasticity calculations based on the SEM images, this work first applies packed DEs (see Figure 3) to discretize digital image pixels. Based on the distinct distribution of grains and clays, as shown in Figure 8, this work usually uses large- and small-sized DEs for cohesive aggregates of grains and clays, respectively. The resulting digital models of DEs are
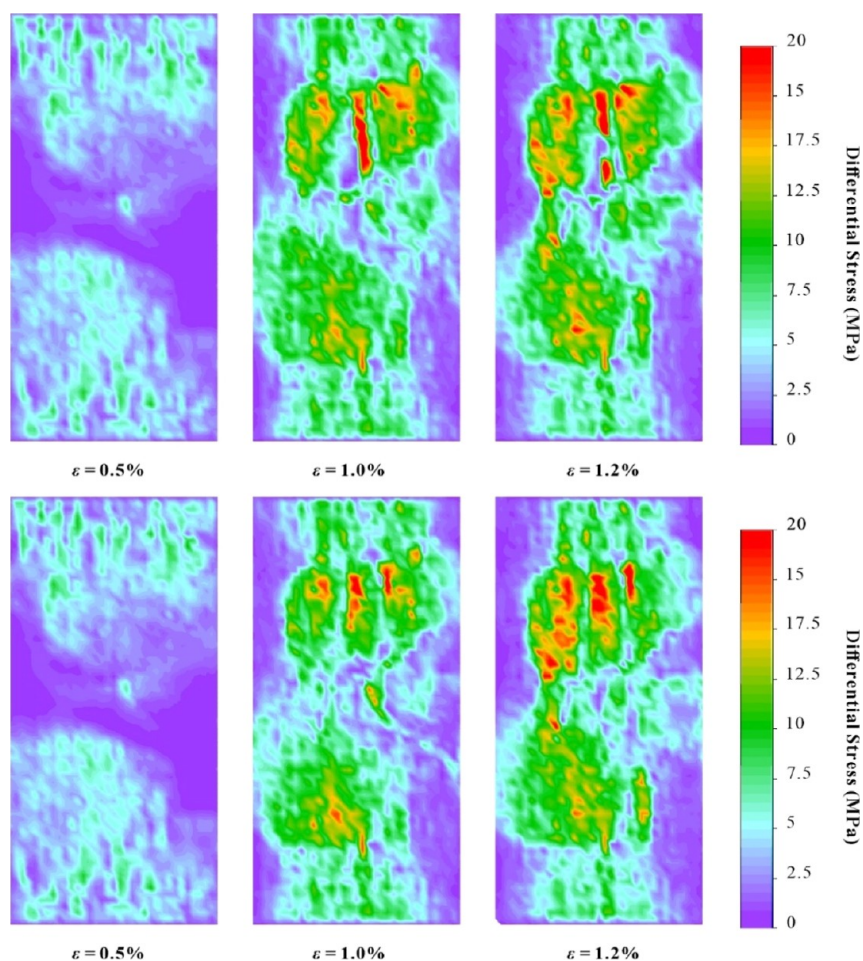
Figure 11. Differential stress fields for model 9 subject to different levels of axial strains (ε = 0.5, 1.0, and 1.2%) under the confinements of 0.5 MPa (upper panel) and 1.0 MPa (lower panel).

shown in Figure 9. Based on the aforementioned statistical analyses of individual voxels, this work can configure petrophysical properties, cement thicknesses, and coordination numbers among these voxels through the parameters *a*, *R*, and *h*. The relevant micromechanical parameters of individual DEs can be adjusted to the mechanical properties of the approximate zone. Particularly, along the boundaries of individual cohesive aggregates of quartz grains, the weakening of grain-clay contacts will be assigned to weakly cemented areas. These loosely cemented areas at the contact boundaries due to a limited compaction will change the distribution of stresses dramatically and in turn affect the effective elastic moduli.

DEM simulations described previously are applied to the digital models of DEs shown in Figure 9. The effective elastic moduli are calculated by applying uniaxial compression experiments. The resulting P- and S-wave velocities are plotted against those (see Table 1) obtained from ultrasonic measurements, as shown in Figure 10. Based on the statistical analyses of petrophysical properties, cement thicknesses, and coordination numbers for individual voxels, this work conducts the CCT and MCCT predictions for these digital models of DEs, which are also plotted against the measured P- and S-wave velocities in Figure 10. Similar to the MCCT prediction, the DEM simulations agree well with the measured values, whereas the CCT model overestimates acoustic velocities for these artificial sandstones because of the assumption of cementation.[38]

4. RESULTS

The elasticity of artificial sandstone samples is examined based on the DEM numerical simulations with biaxial compression tests under the confining pressure. The effects of micro-mechanical characteristics, such as differential stress fields, force chains, and fabric tensors, are numerically investigated based on the confining pressures and applied strain rates. This work demonstrates that biaxial compression tests can help to predict the possible location of stress concentration in the samples.

4.1. Differential Stress Fields. The distribution of stress fields in rocks is significantly altered by elastic interactions of microstructures. This study takes model 9 (see Figure 9) as an example to conduct a series of biaxial experiments. The differential stress is defined as the difference between the maximum and minimum principal stresses experienced by an object. It is often used to estimate the tensile or shear failure determined by the failure criterion.[39] Figure 11 shows the distribution of local differential stresses for the specimen subject to different levels of axial strains (ε = 0.5, 1.0, and 1.2%) under the confinements of 0.5 and 1 MPa, respectively, and represents that both the confinements have similar differential-stress distributions. Unlike well-cemented fractured rocks,[19,40] where the local stress maxima usually occur around fractures, the local stress maxima for weakly cemented sandstones tend to appear inside the cohesive aggregates of grains because these stiff grains have relatively large sizes with loose compaction, whereas stress-
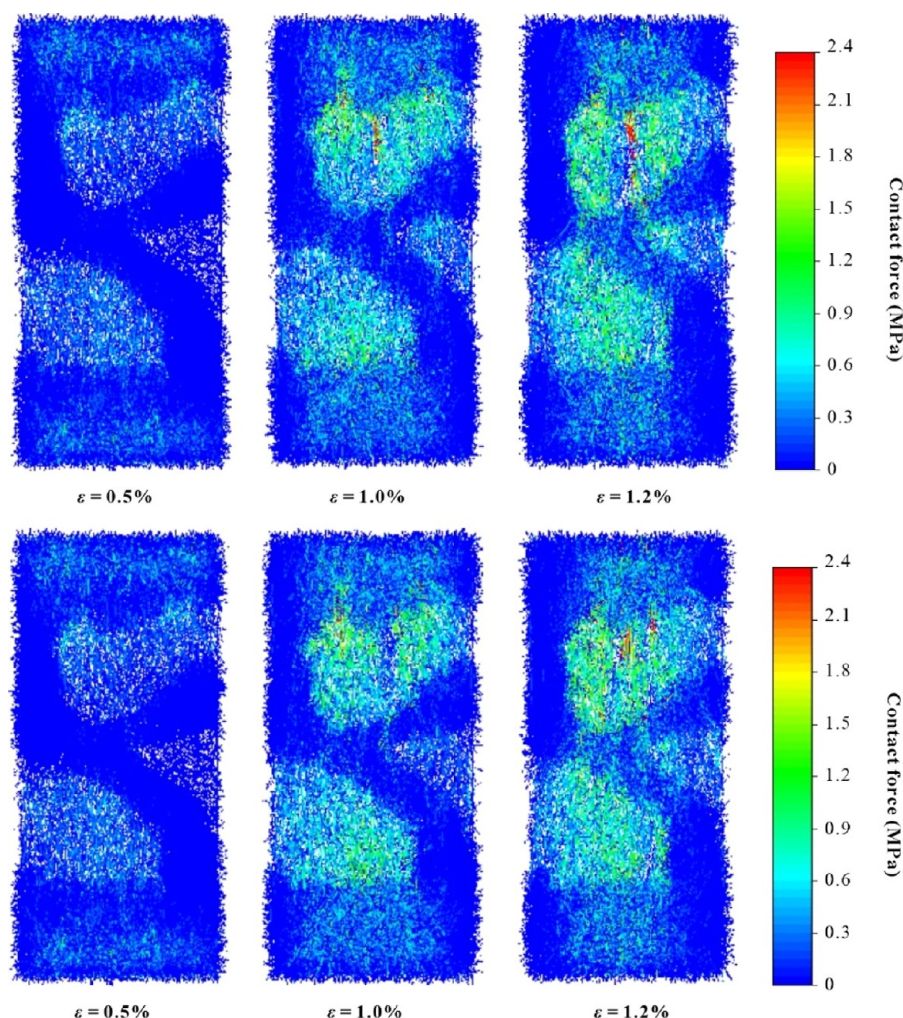
Figure 12. Contact force chains for model 9 subject to different levels of axial strains (ε = 0.5, 1.0, and 1.2%) under the confinements of 0.5 MPa (upper panel) and 1.0 MPa (lower panel).

shielding areas occur around cemented parts due to small soft particles. The stress concentration increases with increasing strains, indicating closer contacts between grains.

4.2. Force Chains. Force chains indicate the contact force between particles in granular media. Such contact forces manifest the transfer path of external loading and connect the macro−micro-mechanical properties of granular media. Based on the DEM numerical simulations with biaxial compression tests, the distribution of force chains across grains can be calculated. Figure 12 shows the evolution of contact forces for model 9 subject to different levels of axial strains (ε = 0.5, 1.0, and 1.2%) under the confinements of 0.5 and 1 MPa, respectively. Similar to the distribution of differential stresses, strong force chains appear inside the matrix because of the loose compaction of large-sized stiff grains, whereas weak force chains are mainly located in the area of clays. The contact forces increase with increasing strains due to increasing external loads, yielding a force-chain buckling inside the matrix that is indicated by a red chain.

4.3. Fabric Tensors. The stress-induced growth of directional features of granular contacts tends to render the medium anisotropic in certain preferential direction. The fabric anisotropy is characteristic of the distribution of directional data, termed fabric tensors.[41] To quantitatively describe the evolution of fabric anisotropy, this study estimate the contact-

normal distribution of model 9 subject to different levels of axial strains (ε = 0.5, 0.8, 1.0, and 1.2%) under the confinements of 1 MPa. Figure 13 shows the rose diagram of directional distributions within the XY-plane of normal forces for mass nodes. Where a_n is the Fourier coefficient, its value represents the anisotropy coefficient of force chain strength, and θ_n is the main direction of chain distribution. The rearrangement of DEs is isotropic in the initial state (ε = 0.5%), with the contact-normal direction uniformly distributed in all directions. With increasing strains, the contact-normal orientation tends to an ellipse with its long axis along the vertical direction, that is, the contact normals concentrate in the direction of the maximum principal stress, whereas the number of contacts decreases in the direction of the minimum principal stress.

5. DISCUSSION

The present work presents a DEM-based numerical study for the elastic behavior of weakly cemented sandstones that are characteristic of loose-bonding contacts, large porosities, and high clay contents. The strength of such rocks depends strongly on intergranular cementations that are most sensitive to deformations due to external loading. Intergranular structures mainly include two typical cemented bonds: contact-bonding and distant-bonding modes. The former has a grain-to-grain direct contact with a small region of cementation and tends to
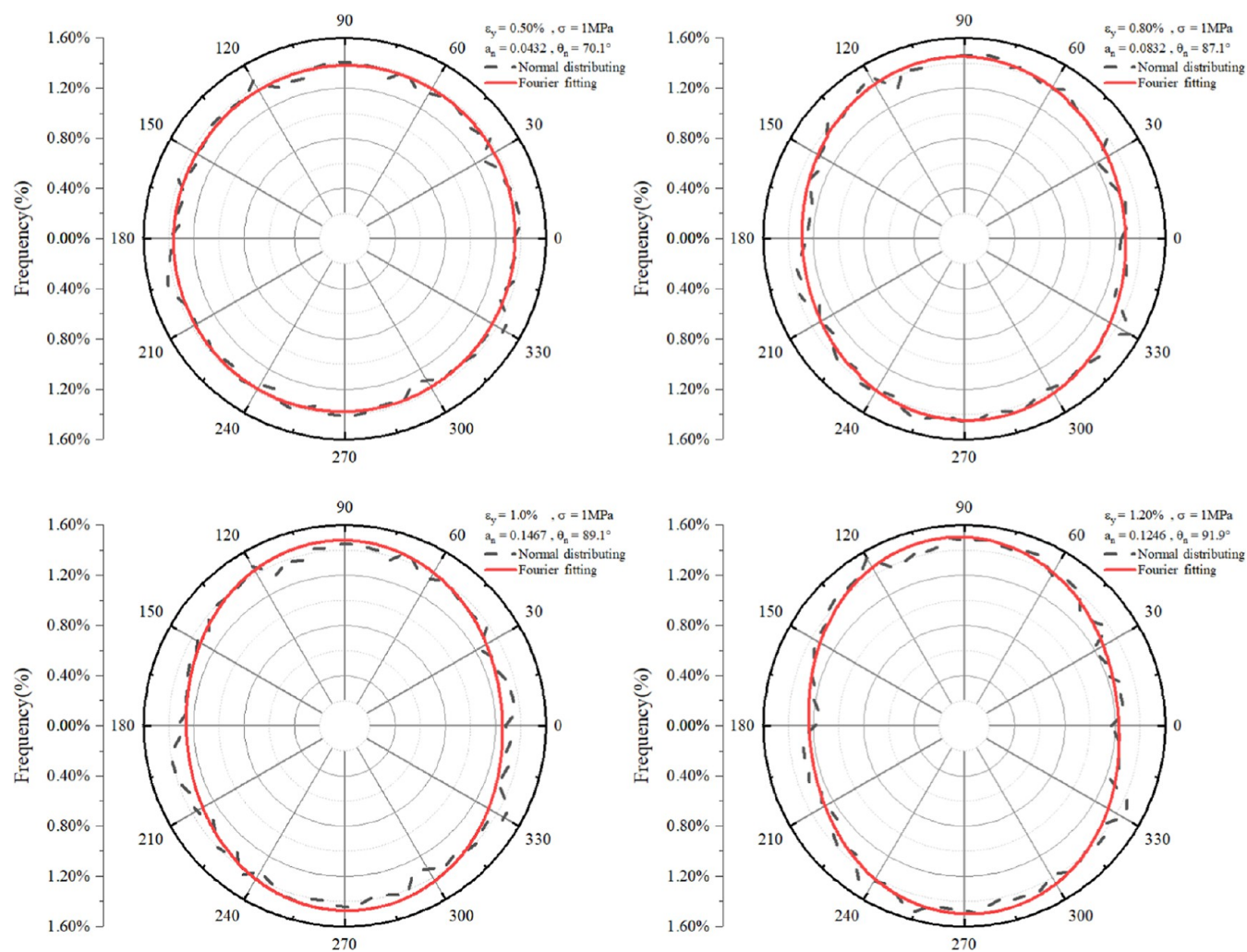
Figure 13. Fabric tensors for model 9 subject to different levels of axial strains (ε = 0.5, 0.8, 1.0, and 1.2%) under the confinements of 1.0 MPa.

overestimate the elastic moduli of weakly cemented sandstones. The latter features noncontacting grains that are joined by a cement bridge that reduces the normal and tangential stiffnesses of grain contacts. Unconsolidated sandstones are usually dominated by such bridging cementation that are controlled by three morphological parameters: cement thickness, bonding radius, and grain radius.

This work employs the built-in parallel bond model in the PFC2D to establish the DEM numerical scheme for the effective elasticity of weakly cemented sandstones. The parallel bond phenomenologically describes the mechanical behavior of intergranular finite-sized cements by a set of normal and shear springs. Unlike the CCT and MCCT models, the contact constitutive relation in the parallel bond is of a wide applicability with flexibility for more complex simulations of granular media. This study randomly packs spherical quartz grains together with adding cements under the specified confining pressure that mechanically stabilizes these packed DEs to ensure the contact-bonding and distant-bonding modes, respectively, followed by repeated uniaxial compression tests to calculate effective elastic moduli. The numerical results are validated by the theoretical CCT and MCCT solutions generally for small contact widths, small contact thicknesses, and large-magnitude moduli, especially for the effective shear modulus.

A series of artificial sandstone samples are made in terms of different proportions of quartz grains and clays (a mixture of epoxy and kaolinite) under loose compaction for weak cementation. The resulting thin-sheet SEM images show cohesive aggregates of grains and clays with different shapes and scales in size. Intergranular contact regions with cements varying in thickness and area manifest both the contact-bonding and distant-bonding modes for weak contacts. The petrophysical properties and morphological parameters can be extracted for DEM simulations by the statistical analysis of individual voxels. The numerical results demonstrate a good agreement with ultrasonic measurements in comparison with the theoretical predictions by CCT and MCCT, where the CCT significantly overestimates acoustic velocities. Numerical investigations for the micromechanical characteristics (differential stress fields, force chains, and fabric tensors) of artificial samples subject to applied axial strains demonstrate that the strong mechanical behavior of weakly cemented sandstones tends to appear inside the cohesive aggregates of stiff grains because of their relatively large sizes with loose compaction.

The DEs do not emulate real grain contacts with distinct angularities, different sizes, and differential adhesive strengths. The assumption and limitations of our DEM simulations are as follows: (i) both grains and cements are assumed to be linear, elastic, and isotropic. (ii) The arrangement of DEs cannot
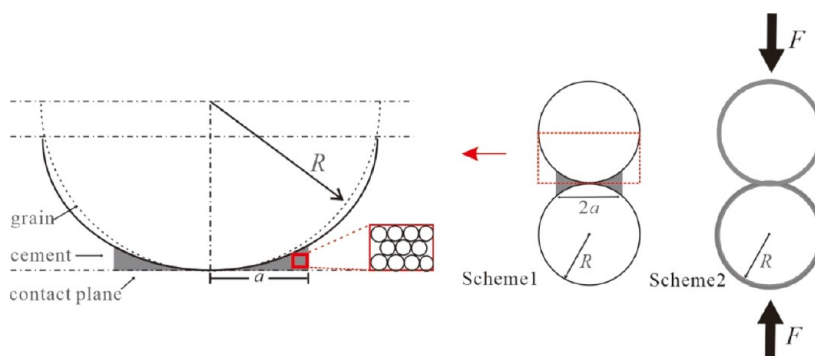
Figure A1. Contact model for the CCT with the cements filled at the grain contacts (Scheme 1) and evenly on the grain surface (Scheme 2).

accurately model individual pores with different sizes, and the cementation is assumed to occur at the grain contacts only. (iii) The DEs phenomenologically replicate the effect of natural cements in the sense of mechanics, without considering local and weak pressure solutions and chemical adhesions at the grain contacts of weakly cemented sandstones.

6. CONCLUSIONS

This study has developed an effective numerical scheme for simulating the cementing medium with high precision. Both contact- and distant-bonding modes of weakly cemented sandstones can be replicated using this approach. In contrast to existing methods, this model is extensible to more complex sandstone samples, demonstrating its potential for quantifying and visualizing internal factors and microscopic mechanisms. Numerical results indicate that the strong mechanical behavior of weakly cemented sandstones tends to manifest within cohesive aggregates of stiff grains due to their relatively large sizes and loose compaction. The correlation between changes in the fine microstructure of cemented sandstone and alterations in macroscopic mechanical properties not only expands the applicability of the DEM to geotechnical problems but also provides a theoretical reference for addressing practical geotechnical challenges.

◾ APPENDIX A

Cemented Contact Models

Dvorkin et al. (1991, 1994)[4,5] present a CCT to describe the normal and tangential deformations of contact-bonding grains for weakly cemented sandstones. The theory predicts the contact stiffness and strength from the geometry of a contact region and allows to calculate the effective elastic moduli of a random packing of spheres.

The contact model used in the CCT is shown in Figure A1, where F, R, and a represent the force applied to the grain, the grain radius, and the radius of cementing region, respectively. The normal and tangential stiffnesses are

$$
\begin{cases}
S_{\mathrm{n}} = -\dfrac{4\pi R G_{\mathrm{c}}(1 - \nu_{\mathrm{c}})}{1 - 2\nu_{\mathrm{c}}} \dfrac{k_{\mathrm{n}}}{\Delta_{\mathrm{n}}} \\[2mm]
S_{\tau} = -2\pi R G_{\mathrm{c}} \dfrac{k_{\tau}}{\Delta_{\tau}}
\end{cases}
\tag{A-1}
$$

with

$$
\begin{cases}
k_{\mathrm{n}} = \displaystyle\int_0^{\alpha} \frac{H_{\mathrm{n}}(t)t\ \mathrm{d}t}{\varepsilon + t^2/2} \\[4mm]
k_{\tau} = \displaystyle\int_0^{\alpha} \frac{H_{\tau}(t)t\ \mathrm{d}t}{\varepsilon + t^2/2}
\end{cases}
\tag{A-2}
$$

where G_{c} denotes the shear modulus of the cement; ν_{c} is Poisson's ratio of the cement; k_{n} and k_{τ} are proportional to the normal force and tangential force, respectively; the normalized cement radius $\alpha = a/R$ indicates the amount of the contact cement, $H_{\mathrm{n}}(t)$ and $H_{\tau}(t)$ denote the normal and tangential deformations of the cement, respectively, and Δ_{n}, and Δ_{τ} represent the overall normal and tangential deformations, respectively.

Based on the effective medium theory,[42] the bulk and shear moduli of weakly cemented sandstones can be calculated from the normal and tangential stiffnesses in A-1

$$
\begin{cases}
K_{\mathrm{eff}} = \dfrac{n(1 - \varphi)}{12\pi R} S_{\mathrm{n}} \\[3mm]
G_{\mathrm{eff}} = \dfrac{n(1 - \varphi)}{20\pi R}\left(S_{\mathrm{n}} + \dfrac{3}{2} S_{\tau}\right)
\end{cases}
\tag{A-3}
$$

where the corresponding P- and S-wave velocities can be denoted as

$$
\begin{cases}
V_{\mathrm{p}}^2 = \dfrac{K_{eff} + 4/3 G_{eff}}{\rho} \\[3mm]
V_{\mathrm{s}}^2 = \dfrac{G_{\mathrm{eff}}}{\rho}
\end{cases}
\tag{A-4}
$$

where φ is the porosity of the loose sandstone, n is the average number of contacts per sphere, K_{eff} and G_{eff} are the bulk and shear moduli, respectively, and V_{p} and V_{s} denote the P- and S-wave velocities, respectively. Dvorkin and Nur (1996)[2] formulate the normalized cement radius by two cases

$$
\alpha = \frac{a}{R} = 2\left[\frac{\varphi_0 - \varphi}{3n(1 - \varphi_0)}\right]^{0.25}
\tag{A-5}
$$

for Scheme 1 with all cements deposited at the grain contacts and

$$
\alpha = \frac{a}{R} = \left[\frac{2(\varphi_0 - \varphi)}{3n(1 - \varphi_0)}\right]^{0.5}
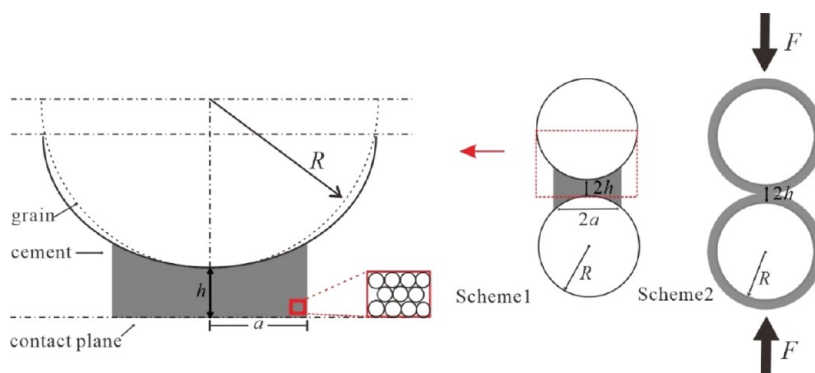\tag{A-6}
$$

Figure A2. Contact model for the MCCT with all cements deposited at the grain contacts (Scheme 1) and evenly on the grain surface (Scheme 2).

for Scheme 2, with all cements deposited evenly on the grain surface, where φ_0 is the critical porosity.

The normal and tangential stiffnesses can be approximated by

$$\begin{cases} S_n = A_n(\Lambda_n)\alpha^2 + B_n(\Lambda_n)\alpha + C_n(\Lambda_n) \\ S_\tau = A_\tau(\Lambda_\tau, \nu)\alpha^2 + B_\tau(\Lambda_\tau, \nu)\alpha + C_\tau(\Lambda_\tau, \nu) \end{cases} \quad (A\text{-}7)$$

with

$$\begin{cases} A_n(\Lambda_n) = -0.024153\cdot\Lambda_n^{-1.3646} \\ B_n(\Lambda_n) = 0.20405\cdot\Lambda_n^{-0.8908} \\ C_n(\Lambda_n) = 0.00024649\cdot\Lambda_n^{-1.9846} \end{cases}$$

and

$$\begin{cases} A_\tau(\Lambda_\tau, \nu) = -10^{-2}\cdot(2.26\nu^2 + 2.07\nu + 2.3)\cdot \\ \qquad\qquad \Lambda_\tau^{0.079\nu^2+0.1754\nu-1.342} \\ B_\tau(\Lambda_\tau, \nu) = (0.0573\nu^2 + 0.0937\nu + 0.202)\cdot \\ \qquad\qquad \Lambda_\tau^{0.0274\nu^2+0.0529\nu-0.8765} \\ C_\tau(\Lambda_\tau, \nu) = -10^{-4}\cdot(9.654\nu^2 + 4.945\nu + 3.1)\cdot \\ \qquad\qquad \Lambda_\tau^{0.01867\nu^2+0.4011\nu-1.8186} \end{cases} \quad (A\text{-}8)$$

where

$$\begin{cases} \Lambda_n = \dfrac{2G_c}{\pi G}\dfrac{(1-\nu)(1-\nu_c)}{1-2\nu_c} \\ \Lambda_\tau = \dfrac{G_c}{\pi G} \end{cases}$$

The CCT model usually holds for high porosity because of the minor amount of cements at grain contacts. Xue-Hui et al. (2014)[8] modify the CCT model for noncontacting grains by proposing a more general expression for the normalized cement radius.

The distant-contact mode used in the MCCT is shown in Figure A2, where h represents the contact thickness. In the MCCT, the normalized cement radius becomes

$$\alpha = \sqrt{-2\varepsilon + 2\sqrt{\varepsilon^2 + \dfrac{4(\varphi_0 - \varphi)}{3n(1-\varphi_0)}}} \quad (A\text{-}9)$$

for Scheme 1 with all cements deposited at the grain contacts and

$$\alpha = \sqrt{\dfrac{2(\varphi_0 - \varphi)}{3(1-\varphi_0)}} \quad (A\text{-}10)$$

for Scheme 2, with all cements deposited evenly on the grain surface, where $\varepsilon = h/R$ is the normalized contact thickness. A-9 reduces to A-10 at $\varepsilon = 0$.

The normal and tangential stiffnesses for the MCCT can be approximated by

$$\begin{cases} S_n = A_n(\Lambda_n, \varepsilon)\alpha^2 + B_n(\Lambda_n, \varepsilon)\alpha + C_n(\Lambda_n, \varepsilon) \\ S_\tau = A_\tau(\Lambda_\tau, \varepsilon)\alpha^2 + B_\tau(\Lambda_\tau, \varepsilon)\alpha + C_\tau(\Lambda_\tau, \varepsilon) \end{cases} \quad (A\text{-}11)$$

where

$$\begin{cases} A_n(\Lambda_n, \varepsilon) = -(5.7792\varepsilon^2 + 0.4569\varepsilon + 0.0446)\cdot \\ \qquad\qquad \Lambda_n^{(105.71\varepsilon^2+5.3505\varepsilon-1.1159)} \\ B_n(\Lambda_n, \varepsilon) = (0.2771\varepsilon^2 + 1.928\varepsilon + 0.2462)\cdot \\ \qquad\qquad \Lambda_n^{(19.307\varepsilon^2+3.3416\varepsilon-0.8023)} \\ B_n(\Lambda_n, \varepsilon) = (0.3939\varepsilon^2 + 0.2114\varepsilon - 0.0018)\cdot \\ \qquad\qquad \Lambda_n^{(-283.46\varepsilon^2+31.128\varepsilon-1.7754)} \end{cases} \quad (A\text{-}12)$$

and

$$\begin{cases} A_\tau(\Lambda_\tau, \varepsilon) = -10^{-2}\cdot(2.26\nu^2 + 2.07\nu + 2.3)\cdot \\ \qquad\qquad \Lambda_\tau^{0.079\nu^2+0.1754\nu-1.342} \\ B_\tau(\Lambda_\tau, \varepsilon) = (0.0573\nu^2 + 0.0937\nu + 0.202)\cdot \\ \qquad\qquad \Lambda_\tau^{0.0274\nu^2+0.0529\nu-0.8765} \\ C_\tau(\Lambda_\tau, \varepsilon) = -10^{-4}\cdot(9.654\nu^2 + 4.945\nu + 3.1)\cdot \\ \qquad\qquad \Lambda_\tau^{0.01867\nu^2+0.4011\nu-1.8186} \end{cases} \quad (A\text{-}13)$$

■ AUTHOR INFORMATION

Corresponding Author

    Xiaoyi Xu − *Institute of Rock and Soil Mechanics, Chinese Academy of Sciences, Wuhan 430071, China;* ◉ orcid.org/0009-0001-7938-1402; Email: xuxiaoyi0924@126.com

Complete contact information is available at:
https://pubs.acs.org/10.1021/acsomega.3c03802

Notes

The author declares no competing financial interest.

REFERENCES

(1) Digby, P. J. The Effective Elastic Moduli of Porous Granular Rocks. *J. Appl. Mech.* **1981**, *48*, 803–808.

(2) Dvorkin, J.; Nur, A. Elasticity of high-porosity sandstones: Theory for two North Sea data sets. *Geophysics* **1996**, *61*, 1363–1370.

(3) Madadi, M.; Christy, A. G. A modified coherent potential approximation: Grain-contact moduli and coordination-number effect. *Geophysics* **2012**, *77*, WA141–WA148.

(4) Dvorkin, J.; Nur, A.; Yin, H. Effective properties of cemented granular materials. *Mech. Mater.* **1994**, *18*, 351–366.

(5) Dvorkin, J.; Mavko, G.; Nur, A. The effect of cementation on the elastic properties of granular material. *Mech. Mater.* **1991**, *12*, 207–217.

(6) Langlois, V.; Jia, X. Acoustic probing of elastic behavior and damage in weakly cemented granular media. *Phys. Rev. E: Stat., Nonlinear, Soft Matter Phys.* **2014**, *89*, 023206.

(7) Langlois, V. Elastic behavior of weakly cemented contact. *Int. J. Numer. Anal. Methods Geomech.* **2015**, *39*, 854–860.

(8) Xue-Hui, H.; Jun-Xin, G.; Feng-Bi, L.; Long, Y. Generalization of the expression of cementation radius in contact cement theory and its application. *Chin. J. Geophys.* **2014**, *57*, 439–449.

(9) Chiu, C. C.; Weng, M. C.; Huang, T. H. Characterization of clastic rock using a biconcave bond model of DEM. *Int. J. Numer. Anal. Methods Geomech.* **2017**, *41*, 422–441.

(10) Theocharis, A.; Roux, J.-N.; Langlois, V. Elasticity of model weakly cemented granular materials: A numerical study. *Int. J. Solids Struct.* **2020**, *193–194*, 13–27.

(11) Lander, R. H.; Walderhaug, O. Predicting Porosity through Simulating Sandstone Compaction and Quartz Cementation. *AAPG Bull.* **1999**, *83*, 433–449.

(12) Avseth, P.; Skjei, N.; Mavko, G. Rock-physics modeling of stress sensitivity and 4D time shifts in patchy cemented sandstones—Application to the Visund Field, North Sea. *Leading Edge* **2016**, *35*, 868–878.

(13) Avseth, P.; Mukerji, T.; Mavko, G.; Dvorkin, J. Rock-physics diagnostics of depositional texture, diagenetic alterations, and reservoir heterogeneity in high-porosity siliciclastic sediments and rocks — A review of selected models and suggested work flows. *Geophysics* **2010**, *75*, 75A31–75A47.

(14) Carcione, J. M.; Gei, D.; Picotti, S.; Qadrouh, A. N.; Alajmi, M.; Ba, J. Rock Acoustics of Diagenesis and Cementation. *Pure Appl. Geophys.* **2022**, *179*, 1919–1934.

(15) Guo, J.; Han, X. Rock physics modelling of acoustic velocities for heavy oil sand. *J. Pet. Sci. Eng.* **2016**, *145*, 436–443.

(16) Madadi, M.; Saadatfar, M. A finite-element study of the influence of grain contacts on the elastic properties of unconsolidated sandstones. *Int. J. Rock Mech. Min. Sci.* **2017**, *93*, 226–233.

(17) Jing, L.; Hudson, J. A. Numerical methods in rock mechanics. *Int. J. Rock Mech. Min. Sci.* **2002**, *39*, 409–427.

(18) Jiang, C.; Zhao, G.-F.; Khalili, N. On crack propagation in brittle material using the distinct lattice spring model. *Int. J. Solids Struct.* **2017**, *118–119*, 41–57.

(19) Liu, N.; Fu, L.-Y. Stress-orientation effects on the effective elastic anisotropy of complex fractured media using the lattice spring models coupled with discrete fracture networks model. *Interpretation* **2020**, *8*, SP31–SP42.

(20) Liu, N.; Fu, L.-Y.; Tang, G.; Kong, Y.; Xu, X. Y. Modified LSM for size-dependent wave propagation: comparison with modified couple stress theory. *Acta Mech.* **2020**, *231*, 1285–1304.

(21) Harthong, B.; Scholtès, L.; Donzé, F.-V. Strength characterization of rock masses, using a coupled DEM-DFN model: *Strength characterization of rock masses. Geophys. J. Int.* **2012**, *191*, 467–480.

(22) Xu, X.; Fu, L.-Y.; Liu, N.; Han, T. On the Determination of Coordination Numbers of Coupled DEM-DFN Model for Modeling Fractured Rocks. *Front. Earth Sci.* **2021**, *9*, 665275.

(23) Mühlhaus, H. B.; Vardoulakis, I. The thickness of shear bands in granular materials. *Geotechnique* **1987**, *37*, 271–283.

(24) Shiu, W.; Donze, F. V.; Daudeville, L. Compaction process in concrete during missile impact: a DEM analysis. *Comput. Concr.* **2008**, *5*, 329–342.

(25) Williams, J. R.; Rege, N. The development of circulation cell structures in granular materials undergoing compression. *Powder Technol.* **1997**, *90*, 187–194.

(26) de Bono, J.; McDowell, G.; Wanatowski, D. Investigating the micro mechanics of cemented sand using DEM. *Int. J. Numer. Anal. Methods Geomech.* **2015**, *39*, 655–675.

(27) Liu, N.; Fu, L.-Y. Elastic Characteristics of Digital Cores from Longmaxi Shale Using Lattice Spring Models. *Commun. Comput. Phys.* **2020**, *28*, 518–538.

(28) Zhao, G.-F.; Russell, A. R.; Zhao, X.; Khalili, N. Strain rate dependency of uniaxial tensile strength in Gosford sandstone by the Distinct Lattice Spring Model with X-ray micro CT. *Int. J. Solids Struct.* **2014**, *51*, 1587–1600.

(29) del Valle-García, R.; Sánchez-Sesma, F. J. Rayleigh waves modeling using an elastic lattice model. *Geophys. Res. Lett.* **2003**, *30*, 1866.

(30) Brendel, L.; Török, J.; Kirsch, R.; Bröckel, U. A contact model for the yielding of caked granular materials. *Granular Matter* **2011**, *13*, 777–786.

(31) Brown, N. J.; Chen, J.-F.; Ooi, J. Y. A bond model for DEM simulation of cementitious materials and deformable structures. *Granular Matter* **2014**, *16*, 299–311.

(32) Scholtès, L.; Donzé, F.-V. A DEM model for soft and hard rocks: Role of grain interlocking on strength. *J. Mech. Phys. Solids* **2013**, *61*, 352–369.

(33) Utili, S.; Nova, R. DEM analysis of bonded granular geomaterials. *Int. J. Numer. Anal. Methods Geomech.* **2008**, *32*, 1997–2031.

(34) Shen, Z.; Jiang, M.; Thornton, C. DEM simulation of bonded granular material. Part I: Contact model and application to cemented sand. *Comput. Geotech.* **2016**, *75*, 192–209.

(35) Camusso, M.; Barla, M. Microparameters Calibration for Loose and Cemented Soil When Using Particle Methods. *Int. J. Geomech.* **2009**, *9*, 217–229.

(36) Liu, S. H.; Sun, D. A. Simulating the collapse of unsaturated soil by DEM. *Int. J. Numer. Anal. Methods Geomech.* **2002**, *26*, 633–646.

(37) Han, X.; Xu, D.; Guo, J.; et al. Rock physics modelling for acoustic velocities of sandstone considering effects of cementation and compaction. *Chin. J. Geophys.* **2018**, *61*, 5044–5051.

(38) Avseth, P.; Johansen, T. A.; Bakhorji, A.; Mustafa, H. M. Rock-physics modeling guided by depositional and burial history in low-to-intermediate-porosity sandstones. *Geophysics* **2014**, *79*, D115–D121.

(39) Liu, N.; Li, M.; Chen, W. Mechanical deterioration of rock salt at different confinement levels: A grain-based lattice scheme assessment. *Comput. Geotech.* **2017**, *84*, 210–224.

(40) Liu, N.; Fu, L.-Y. Modeling seismic responses in complex fractured media using the modified lattice spring model coupled with discrete fracture networks. *J. Nat. Gas Sci. Eng.* **2021**, *95*, 104206.

(41) Cowin, S. C. Anisotropic poroelasticity: fabric tensor formulation. *Mech. Mater.* **2004**, *36*, 665–677.

(42) Winkler, K. W. Contact stiffness in granular porous materials: Comparison between theory and experiment. *Geophys. Res. Lett.* **1983**, *10*, 1073–1076.